

Research Article

Megavoltage X-Ray Imaging Based on Cerenkov Effect: A New Application of Optical Fibres to Radiation Therapy

A. Teymurazyan¹ and G. Pang^{1, 2, 3, 4}

¹Imaging Research, Sunnybrook Health Sciences Centre and Department of Medical Biophysics, University of Toronto, Toronto, ON, Canada M4N 3M5

²Odette Cancer Centre, Toronto, ON, Canada M4N 3M5

³Department of Radiation Oncology, University of Toronto, Toronto, ON, Canada M5G 2M9

⁴Department of Physics, Ryerson University, Toronto, ON, Canada M5B 2K3

Correspondence should be addressed to A. Teymurazyan, teymuraz@sri.utoronto.ca

Received 14 July 2011; Revised 19 September 2011; Accepted 20 September 2011

Academic Editor: Baohong Yuan

Copyright © 2012 A. Teymurazyan and G. Pang. This is an open access article distributed under the Creative Commons Attribution License, which permits unrestricted use, distribution, and reproduction in any medium, provided the original work is properly cited.

A Monte Carlo simulation was used to study imaging and dosimetric characteristics of a novel design of megavoltage (MV) X-ray detectors for radiotherapy applications. The new design uses Cerenkov effect to convert X-ray energy absorbed in optical fibres into light for MV X-ray imaging. The proposed detector consists of a matrix of optical fibres aligned with the incident X rays and coupled to an active matrix flat-panel imager (AMFPI) for image readout. Properties, such as modulation transfer function, detection quantum efficiency (DQE), and energy response of the detector, were investigated. It has been shown that the proposed detector can have a zero-frequency DQE more than an order of magnitude higher than that of current electronic portal imaging device (EPID) systems and yet a spatial resolution comparable to that of video-based EPIDs. The proposed detector is also less sensitive to scattered X rays from patients than current EPIDs.

1. Introduction

Radiation therapy is widely used today to treat patients with tumors [1]. Megavoltage (MV) X-ray beams generated from a linear accelerator are commonly used to deliver the prescribed radiation dose to the tumor while minimizing the dose to the surrounding healthy tissues. The geometric accuracy of such treatment is crucial for its success. Currently, there are a number of ways to verify the positional accuracy of the treated target. One of them is to use MV cone beam CT (MV-CBCT) to locate the position of the target in the treatment room prior to the start of the treatment [2, 3]. MV-CBCT uses an electronic portal imaging device (EPID) [4] attached to the LINAC to acquire CT data by rotating the MV X-ray source (emitting a cone beam) and the EPID around the patient. One of the main challenges with this approach is that the imaging dose currently required to achieve sufficient soft tissue contrast to visualize and delineate a soft tissue target; for example, the prostate is prohibitively large for daily

verification. This is due to the poor X-ray absorption, that is, low quantum efficiency (QE) of the EPID used. For most EPIDs developed so far, the QE is typically on the order of 2–4% at 6 MV as compared to the theoretical limit of 100% [5]. This is because the total combined thickness of the energy conversion layer and the metal buildup in most EPIDs is only ~2 mm. In contrast, the first half value layer (HVL) for 6 MV X-ray beams is ~13 mm of lead. Thus, a significant increase of QE is required in order to reduce the dose currently required to visualize and delineate the prostate using MV-CBCT.

Efforts were made previously to build high QE area detectors for MV X-ray imaging in radiotherapy, including (1) the use of a thick CsI(Tl) scintillator to replace the thin phosphor screen in a mirror video-based system [6], (2) the use of solid converters and a gas electron multiplier to detect MV X rays [7], (3) the use of brass tubes filled with gas to detect MV X rays [8], (4) the use of scintillating crystal matrix to replace the phosphor screen in an indirect flat panel [9–11],

and (5) the use of a large number of microstructured plates (with W converters, microsize cavities filled with Xe, and microstrip electrodes) packed together to achieve a QE of up to $\sim 60\%$ [12]. However, all of these detectors are made of high atomic number (high-Z) materials, which results in a severe overresponse of the EPIDs to low-energy scattered X rays [13, 14].

Recently, this research group introduced a new design of a high QE area detector made of low-Z materials for MV X-ray imaging in radiation therapy [15]. It is based on Cerenkov radiation [16]. Cerenkov radiation (or Cerenkov light) is an electromagnetic “shock-wave” of light produced by a charged particle passing through a dielectric medium with a velocity greater than the speed of light *in the medium*. Figure 1 shows a cross-section of our proposed system (subsequently referred to as Cerenkov portal imaging detector or CPID). It consists of a large area and thick (thickness $d \sim 10\text{--}30\text{ cm}$) fibre-optical taper (FOT) directly coupled to an optically sensitive 2D active matrix flat panel imager (AMFPI). The active matrix is made optically sensitive either with an *a*-Si PIN photodiode at every pixel or a continuous layer of amorphous selenium (*a*-Se) [17]. We note that AMFPI using *a*-Si PIN photodiodes has been used in current low-QE EPIDs for many years, and no significant image artifact due to the nonuniform structure of AMFPI has been found in clinical images [4]. It has also been shown that AMFPI is highly resistant to radiation [18]. The FOT is a matrix of optical fibres, each of which has a diameter of several hundred micrometers and is aligned with the incident X rays (i.e., focused towards the X-ray source) to avoid blur due to oblique incidence of off-axis X rays (Figure 1(a)). This focusing towards the X-ray source can be achieved by an extra coating at the bottom of the otherwise uniform fibres. When MV X rays interact with the FOT, energetic electrons will be produced. Those electrons with energy greater than the threshold energy ε_C required for Cerenkov radiation in the fibre material will produce Cerenkov light along their tracks. The light photons produced in a fibre core and emitted within the acceptance angle of the fibre will be guided towards the optical detector, that is, the *optically sensitive AMFPI*, by total internal reflection. The *a*-Se layer (or *a*-Si PIN photodiodes) in the optical detector can in principle be operated in the avalanche mode [19] if necessary to amplify the signal in order to overcome the electronic noise in the active matrix readout.

In this paper, we investigate the feasibility of the new design (i.e., CPID) using Monte Carlo simulation. We have simulated properties of the CPID, such as detection efficiency, modulation transfer function, and energy dependence. The results of our study, presented in this paper, merit the use of optical fibres for MV X-ray imaging applications in radiation therapy.

2. Methods and Materials

2.1. Processes and Cuts Considered in the Monte Carlo Simulation Program. The simulation program, developed to study the imaging and dosimetric characteristics of the proposed

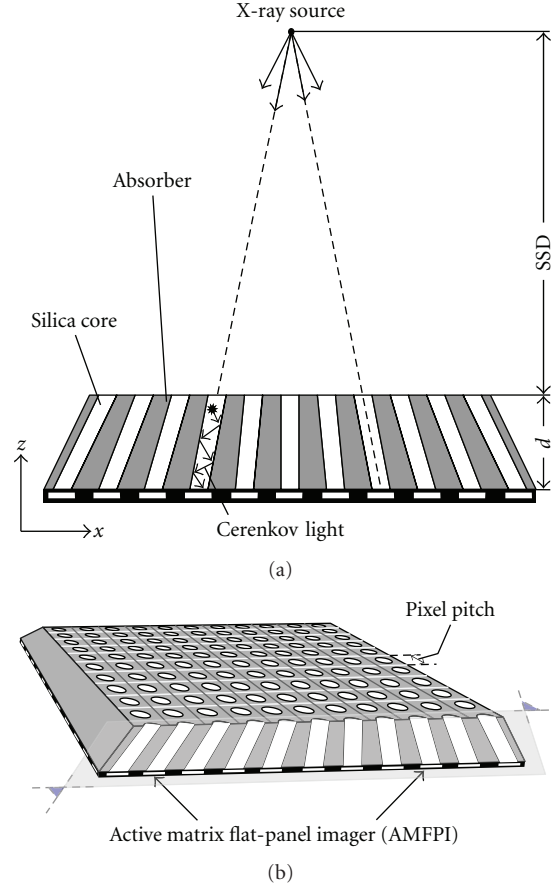


FIGURE 1: Schematic illustration of the proposed CPID. (a) a small cross section of the detector and (b) a 3D view of a small portion of the detector. The detector contains 931×931 pixels in the actual simulation.

CPID under irradiation of MV X rays, is based on the Geant4 toolkit (version 9.3 patch-01). The Geant4 toolkit contains physics models covering the interactions of most particle types over a wide energy range (down to 1 keV and below) [20]. Unlike most general-purpose Monte Carlo codes, describing propagation of radiation in matter, it also includes models describing the transport and boundary processes for optical photons. In Geant4 framework, optical photons can be produced by scintillation, Cerenkov effect, or wavelength shifting [20]. For the detector considered in this work, the optical photons are generated by Cerenkov effect only.

The list of particles considered in simulation consists of photons, electrons, positrons, and optical photons. The list of physics processes controlling the particle interactions in the simulation, that is, photoelectric effect, Compton scattering, e^+e^- -pair production, Rayleigh scattering, multiple scattering, ionization, bremsstrahlung, annihilation, is largely based on the *standard EM* (electromagnetic) *physics list* supplied with Geant4 distribution (class name *G4EmStandardPhysics_option3*). The EM list was extended to include generation of optical photons via Cerenkov effect. The simulation accounts for optical photon interactions such

as bulk absorption, optical Rayleigh scattering, and optical boundary processes, that is, reflection and refraction [20].

Other modifications to the default parameters of the predefined physics list include the increased number of bins in stopping power ($S(E) = -dE/dx$) and inverse interaction length ($\lambda(E)$) tables from its default value of 220 to 480 bins. The Geant4 applications have a built in, user controllable, production thresholds for secondary particles. These were set to 4.5 mm and 0.16 mm for photons, positrons and electrons, respectively.

2.2. Detector Configuration as Modeled in Simulation. A schematic illustration of the proposed detector is given in Figure 1. The active components are fused silica fibres focused towards the X-ray source to avoid blurring due to oblique incidence of off-axis X rays.

The gap between fibres is filled with an opaque material (e.g., water-equivalent black resin) to absorb light that is not guided by the fibres but instead escapes from the side of the fibres. This optically opaque medium, which will subsequently be referred to as the *absorber*, also acts as an energy converter for X rays that would otherwise pass between the fibres without interaction. Furthermore, the absorber reduces the effective range of the electrons (and positrons) generated in the detector, and thus, improves the spatial resolution as well.

The fused silica fibres used in the simulation are cylindrical, each with a fibre core diameter of 0.4 mm and a cladding layer thickness of 0.015 mm, resulting in an outer diameter of 0.43 mm for the whole fibre. The gap between adjacent fibres at the top surface of the detector is 0.005 mm, leading to a pixel pitch of $0.435 \times 0.435 \text{ mm}^2$ (see Figure 1(b)). The matrix of fused silica fibres contains a total of 931×931 elements. The whole detector has a shape of truncated pyramid with optical fibres embedded in the absorber. The total area for the top surface of the detector facing the X-ray source is $40.455 \times 40.455 \text{ cm}^2$ and the source-to-detector surface distance (SSD) is 157 cm (see Figure 1). The length of the fused silica fibres or the thickness d of the detector is a variable parameter that primarily influences the QE of the detector. Detector thicknesses of up to 30 cm have been simulated.

2.3. Detector Materials Considered in the Simulation. The clear optical fibres for X-ray detection via Cerenkov effect are modeled having a fused silica core (density of 2.201 g cm^{-3} and refractive index of $n_{\text{core}} \approx 1.46$). The amount of the light captured and transmitted in fibres depends on the numerical aperture (NA) of the fibre: $\text{NA} = \sqrt{n_{\text{core}}^2 - n_{\text{cladding}}^2}$. The numerical aperture of the fibre depends on the cladding material and can range from ~ 0.22 to 0.66 (e.g., see technical specifications for fused silica core fibres by Polymicro Technologies LLC). In our simulations, we used $\text{NA} = 0.48$ (a value characteristic of FSHA fibres by Polymicro Technologies LLC). Fused silica and Teflon have been considered for cladding material in the simulation (as the information on the proprietary polymer cladding for FSHA fibre is unavailable). For fused silica core fibres,

the characteristic absorption length over which a signal is attenuated to $1/e$ of its original value is ~ 20 – 100 m (for 365 – 800 nm wavelengths). Hence, the absorption of optical photons in fibre cores is a small effect for physical lengths of up to $\sim 30 \text{ cm}$. Nevertheless, it was taken into account in the simulation.

The absorber medium between the fibres is assumed to be 100% opaque. The X-ray interaction properties of the water-equivalent black resin are assumed to be the same as that of water in the simulation.

The CPID is simulated as positioned in the center of a $10 \times 10 \times 10 \text{ m}^3$ volume of air. The primary X rays originate and travel in an air-full environment before reaching the detector.

If not specified, the definitions of all the materials used in the simulation, single element or compound, are taken from the Geant4/NIST materials database.

2.4. Physics Processes in Detector during Irradiation. When MV X rays are incident on the CPID, they interact with the optical fibres and the absorber medium in the detector primarily via Compton effect and e^+e^- -pair production, yielding energetic charged particles (electrons and positrons). From these charged particles, those with sufficient kinetic energy will trigger production of Cerenkov light while traveling in fused silica fibre cores [16]. The light photons, which are produced in a fibre core and emitted within the acceptance angle of the fibre are guided towards the AMFPI by total internal reflection. The light signal that reaches the AMFPI is then converted to an electronic signal and read out by the AMFPI.

Cerenkov Effect. The threshold kinetic energy of a charged particle, above which Cerenkov radiation will be generated, can be expressed in terms of refractive index n of the dielectric medium and the rest mass m_0 of the charged particle:

$$\varepsilon_C = m_0 c^2 \left(\frac{n}{\sqrt{n^2 - 1}} - 1 \right), \quad (1)$$

where c is the speed of light in vacuum. In silica, electrons or positrons with energy higher than $\sim 190 \text{ keV}$ will generate Cerenkov light. The simulation takes into account the generation of Cerenkov radiation in the fused silica fibre cores for wavelengths between 365 – 800 nm . Production of Cerenkov radiation in other components of the detector is negligible due to their opacity or smaller volumes.

2.5. Simulated Detector Quantities. The simulation tracks individual histories of all particles: primary, secondary, as well as optical photons, and the energy deposited in the core of each fibre is summed for all tracks and tallied on event-by-event basis. The number of Cerenkov photons created and ones escaping the bottom end of each fibre core is scored on event-by-event basis. Note that an event in the simulation is defined as an instance of an individual X ray and all of its secondaries being tracked through the whole detector.

To study the imaging and dosimetric characteristics of the CPID for clinically relevant X-ray beams, X-ray

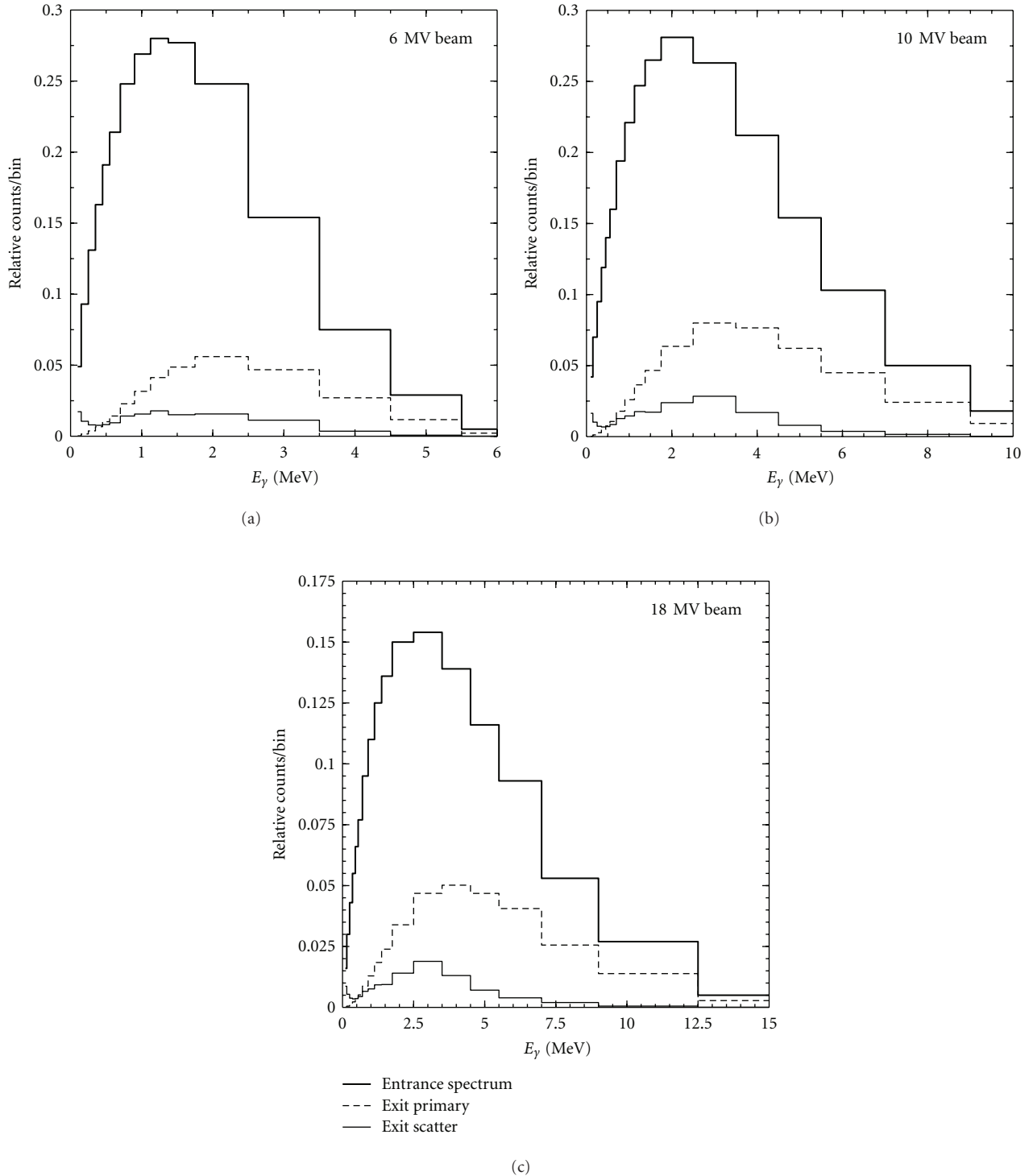


FIGURE 2: X-ray spectra used in the simulation. The entrance spectrum was generated by a treatment planning system (Pinnacle3, Philips), and the exit spectra of X rays were simulated by passing the incident beam (with the entrance spectrum) through a 30 cm thick water phantom.

energy spectra (see Figure 2, entrance spectra) for clinical machines generated by a treatment planning system (Pinnacle3, Philips) were used in the simulation in addition to monoenergetic X-ray beams. For mono-energetic X-ray beams, the energy was varied between 0.2 and 20 MeV.

2.5.1. Beam Energy Hardening and Scatter due to the Presence of a Patient. During imaging a patient is positioned between the X-ray source and the EPID. The presence of patient both (1) alters the spectrum of primary X rays exiting the patient and (2) results in generation of secondary particles (X rays,

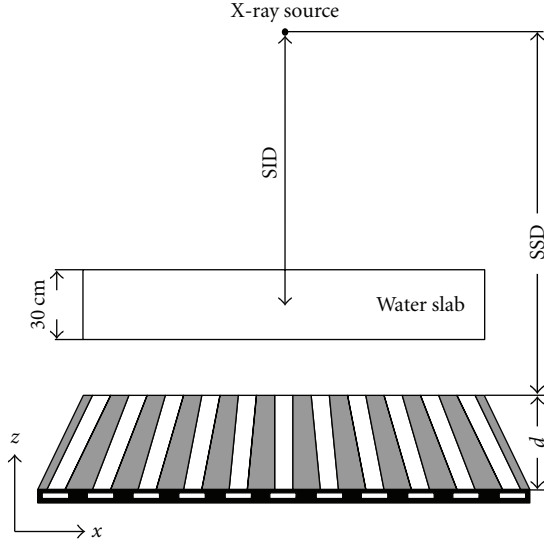


FIGURE 3: Schematic illustration of the geometry used when simulating the primary and scatter components of exit beam due to the presence of a “patient.”

electrons, and positrons) from the patient. To obtain the energy spectra for primary and scattered components of exit beam, the simulation configuration shown in Figure 3 was used. The patient was modeled as a 30 cm thick water slab (phantom) at the isocenter ($SID = 100$ cm), and the energies and the angles of exit particles were recorded at the detector plane ($SSD = 157$ cm). A pencil beam sampling the entrance energy spectrum was used to simulate the primary (i.e., nonscattered) and scatter components of exit beam. In our simulations, we investigated the CPID response in absence of a patient (using the entrance spectra from Figure 2) as well as the response in presence of a “patient” (using the energy spectra for scattered and primary components of exit beam).

2.5.2. Spatial Resolution. The spatial resolution of the detector can be expressed by the modulation transfer function (MTF) [21]. The one-dimensional MTF is the Fourier transform of the line-spread function [5, 22], that is,

$$MTF(f) = \int_{-\infty}^{\infty} e^{-2\pi i x f} LSF(x) dx, \quad (2)$$

where the line spread function $LSF(x)$ is defined as

$$LSF(x) = \int_{-\infty}^{\infty} n(x, y) dy. \quad (3)$$

Here $n(x, y)$ is the point-spread function or the distribution of optical photons that escape the fibres and reach the AMFPI under the irradiation of an infinitely small-size pencil beam. Note that spatial frequencies in this work are referenced to the top surface of the CPID.

To overcome the sampling limitation as in any digital system [12, 21, 23], we varied the location of the incident beam with respect to the detector in the X direction (Figure 1) with a step size of $53.75 \mu\text{m}$ and sampled over all uniformly

distributed locations within a detector pixel [23]. Prior to applying the Fourier transformation to obtain the MTF, the values of LSF between sampling locations were calculated by linear interpolation. We have also calculated the MTF using a finite-size ($0.435 \times 0.435 \text{ mm}^2$) pencil beam, and the result was essentially identical to that using the infinitely small-size pencil beam.

2.5.3. CPID Response. The total mean signal of the detector per pixel under irradiation with X rays of a given energy E_γ can be expressed as a product of the probability of an incident X ray to be detected in CPID $\eta(E_\gamma)$ (detection efficiency), the mean number of the optical photons reaching the AMFPI per detected X ray $r(E_\gamma)$ and the incident fluence of X rays $\Phi(E_\gamma)$; namely,

$$R(E_\gamma) = A_d \eta(E_\gamma) r(E_\gamma) \Phi(E_\gamma). \quad (4)$$

Here we assume X-ray fluence from an isotropic point source is incident on the detector, and $\Phi(E_\gamma)$ represents the total (primary and scattered) fluence reaching a pixel with area A_d .

Pixel-sized (i.e., $0.435 \times 0.435 \text{ mm}^2$) pencil beams normally incident at the center of the top surface of the detector were used to simulate the CPID response. Taking advantage of the geometry of the detector, the number of Cerenkov photons reaching the AMFPI was integrated over all fibres on an event-by-event basis to obtain the detector signal per pixel.

Detection Efficiency. When MV X rays are incident on the CPID, not all of them interact with the detector and generate a signal in the detector. The detection efficiency $\eta(E_\gamma)$ is defined as the probability of an incident X ray to produce at least one Cerenkov photon that is guided by the fibre matrix and reaches the AMFPI, irrespective of the position of interaction of the primary X ray in the detector. Throughout this work we assume that the matrix of optical fibres and AMFPI have 100% optical coupling efficiency, and any optical photon incident on the AMFPI will generate an electronic signal in the AMFPI. As such, the detection efficiency quantifies the ability of the CPID to utilize the incident X-ray fluence. We note here that the detection efficiency is equal to or lower than the QE, which is defined as the percentage of incident X rays interacting with the detector. Thus, a high detection efficiency means a high QE.

Detector Sensitivity. The quantity $r(E_\gamma)$, introduced in (4), represents the efficiency with which the detected X rays are converted into optical photons. The product of $r(E_\gamma)$ and $\eta(E_\gamma)$ gives the mean number of optical photons reaching the AMFPI per incident X-ray on the detector, that is, the detector sensitivity. The dependence of detector sensitivity on the energy of incident X rays describes the energy response function of the detector.

Signal Scatter Fraction. The presence of a patient, in the beam, results in generation of secondary scattered particles that generally degrade image quality. The contribution to

the total signal per detector pixel from secondary particles is typically presented in form of signal scatter fraction [24]:

$$SF_{\text{signal}} = \frac{\bar{R}_s}{\bar{R}_s + \bar{R}_p}, \quad (5)$$

where \bar{R}_s and \bar{R}_p are the mean signals per pixel due to scattered and primary components of exit beam from the patient, respectively. To further assess the effect of patient scatter on detector performance, we have also calculated the point spread function $n(x,y)$ in presence of a ‘‘patient’’ (with the pencil beam incident on the ‘‘patient’’) in comparison with that without a patient.

2.5.4. Detective Quantum Efficiency. The *detective quantum efficiency* (DQE) is a measure of the image quality of an X-ray detector. The zero spatial frequency DQE of an imaging system can be expressed as [14, 25, 26]

$$DQE(0) = \frac{M_1^2}{M_2}, \quad (6)$$

where M_n , the n th moment of the distribution $p(m)$ of the number m of optical photons reaching the AMFPI normalized to the number of incident X rays, N_X :

$$M_n = \frac{1}{N_X} \sum_m m^n p(m). \quad (7)$$

We note that by definition $\eta = M_0$, $r = M_1/M_0$ and $N_X = A_d\Phi$.

The stochastic nature of interaction of radiation with mater gives rise to the distribution of number of optical photons. For a Cerenkov effect-based detector, the shape of $p(m)$ is dictated by the distribution of energies of electrons and positrons and their angles with respect to the fibre cores [15]. The general form of (6) and (7) is valid both for discrete X-ray energies and for X-ray energy spectra. In our simulations, we directly sampled the X-ray energy spectra (see Figure 2) to obtain the distribution of the number of optical photons $p(m)$ for clinical X-ray beams. However, the same result could be produced by averaging the respective moments M_n (obtained for discrete X-ray energies) over the X-ray energy spectrum. The results for DQE presented in this paper include not only the X-ray quantum absorption noise, but also noise due to variations in Cerenkov light production and transport in fibre cores.

Finally, in case when the noise is white (i.e., frequency independent), the spatial-frequency-dependent DQE(f) is given by [27]

$$DQE(f) = DQE(0) \cdot |\text{MTF}(f)|^2, \quad (8)$$

where $\text{MTF}(f)$ is the modulation transfer function (see Section 2.5.2).

2.5.5. Energy Dependence of CPID Dose Response. To assess the water equivalence of the detector at a given X-ray energy E_γ , we define a ratio $\alpha(E_\gamma)$ of the value of detector sensitivity

$r(E_\gamma)\eta(E_\gamma)$ to the absorbed dose $\Gamma(E_\gamma)$ per incident fluence $\Phi(E_\gamma)$. Namely,

$$\alpha(E_\gamma) = \frac{\eta(E_\gamma)r(E_\gamma)\Phi(E_\gamma)}{\Gamma(E_\gamma)}, \quad (9)$$

where the definition and calculation of $\Gamma(E_\gamma)$ is given below (see Section 2.6). For ease of representation, the detector response per unit dose (deposited in water) was normalized to its value at a fixed energy of incident X rays. The value of 2 MeV was chosen as the reference X-ray energy in the analysis, and $\alpha(E_\gamma)/\alpha(2 \text{ MeV})$ is defined as the *relative response* of the detector to X-ray at a discrete energy for a fixed dose to water. For polyenergetic X-ray beams (see Figure 2), the detector sensitivity $r(E_\gamma)\eta(E_\gamma)$ and the absorbed dose per incident fluence $\Gamma(E_\gamma)/\Phi(E_\gamma)$ are separately averaged over the X-ray energy spectrum prior to calculating the relative response.

2.6. Dose to Water and Fluence-to-Dose Conversion Factors. The absorbed dose $\Gamma(E_\gamma)$, in (9), is defined as the mean dose absorbed in a water slab of an equivalent thickness d' as if the whole detector were made of pure water; that is,

$$\Gamma(E_\gamma) = \frac{1}{d'} \int_0^{d'} D(E_\gamma, z) dz, \quad (10)$$

where $D(E_\gamma, z)$ is the dose in water at depth z [1].

Figure 4 shows the fluence-to-dose conversion factors $\Gamma(E_\gamma)/\Phi(E_\gamma)$, assuming a broad parallel beam of normal incidence, for water slab in air environment. The data used in Figure 4 is listed in Table 1. A Geant4-based simulation was developed to calculate the depth-dose curves in a water phantom in presence of surrounding air. It considers a slab of water with surface area of $300 \times 300 \text{ cm}^2$ and thickness d' situated in a $10 \times 10 \times 10 \text{ m}^3$ volume of air. The water slab is logically divided, that is, without physical gaps, into 1 mm thick slices along its depth axis Z . The depth-dose curves for a broad parallel beam of primary X rays were obtained by considering a pencil beam of $1 \times 1 \text{ mm}^2$ normally incident on the surface of the water slab. The total energy deposited per unit areal density is scored in a millimeter-thick water slabs at each depth, which gives the depth-dose curve $D(E_\gamma, z)$. The primary X rays travel a source-to-surface distance of 157 cm in air.

The CPID thicknesses ($d = 10, 20, \text{ and } 30 \text{ cm}$) investigated in this paper were scaled by the mean physical densities of the detector to obtain the equivalent thicknesses ($d' = 18.67, 36.30, \text{ and } 53.01 \text{ cm}$) of water slabs needed to calculate $\Gamma(E_\gamma)$.

3. Results

3.1. Spatial Resolution. The modulation transfer functions (MTFs) of the CPID for various detector thicknesses d at 6 MV and 10 MV are shown in Figure 5. The entrance spectra from Figure 2 were used in the simulation. It can be seen that the MTF of the detector decreases at all frequencies with the

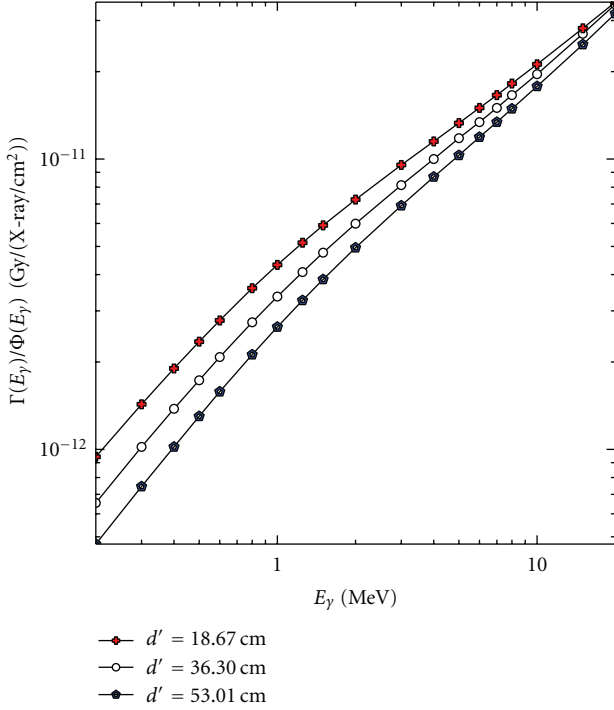


FIGURE 4: Fluence-to-mean-dose-in-water conversion factors $\Gamma(E_y)/\Phi(E_y)$ used in calculating the energy response of CPID. The mean dose in water is defined as the integral of depth-dose curve along the depth axis normalized to the thickness of the water slab. The calculations assume broad parallel beam of X rays incident normally on 18.67, 36.30, and 53.01 cm thick slabs of water in air.

increase of the detector thickness, which is due to an increase of X-ray scatter in a thicker detector [5].

Figure 6 shows the values of f_{50} (i.e., the frequency at 50% of the MTF) as a function of the detector thickness for different beam qualities. The value of f_{50} at $d = 10$ cm for a 6 MV clinical beam is ~ 0.24 lp/mm, which is comparable to that of video-based EPIDs ($f_{50} \sim 0.2$ lp/mm) [4]. A reduction of $\sim 20\%$ of f_{50} was observed in our simulations when increasing the detector thickness to $d = 30$ cm.

3.2. CPID Response

3.2.1. Detection Efficiency. Figure 7 shows the detection efficiencies of the CPID for various detector thicknesses as a function of incident X-ray energy. The efficiency for detecting X rays by means of the Cerenkov effect decreases rapidly with the decrease of X-ray energy below ~ 1 MeV due to the threshold kinetic energy required to generate the Cerenkov light.

For clinically relevant X-ray spectra at 6, 10, and 18 MV (see entrance spectra in Figure 2), the detection efficiencies of CPID for various detector thicknesses are given in Table 2, which are more than an order of magnitude higher than that of current EPIDs.

3.2.2. Detector Sensitivity. The number of optical photons that are generated in the detector and reach the AMFPI per

TABLE 1: X-ray fluence-to-mean-dose conversion factors for monoenergetic broad parallel beams incident on 18.67, 36.30, and 53.01 cm thick water slabs in air in units of Gy/(X-ray/cm²). Statistical uncertainties for each X-ray energy are 1.2%, 1.3%, and 1.3% for the 18.67, 36.30, and 53.01 cm thick water slabs, respectively.

| E_y/MeV | $d' = 18.67$ cm | $d' = 36.30$ cm | $d' = 53.01$ cm |
|------------------|------------------------|------------------------|------------------------|
| 0.2 | 9.43×10^{-13} | 6.54×10^{-13} | 4.72×10^{-13} |
| 0.3 | 1.43×10^{-12} | 1.02×10^{-12} | 7.45×10^{-13} |
| 0.4 | 1.90×10^{-12} | 1.38×10^{-12} | 1.02×10^{-12} |
| 0.5 | 2.35×10^{-12} | 1.73×10^{-12} | 1.30×10^{-12} |
| 0.6 | 2.78×10^{-12} | 2.08×10^{-12} | 1.58×10^{-12} |
| 0.8 | 3.59×10^{-12} | 2.74×10^{-12} | 2.12×10^{-12} |
| 1 | 4.32×10^{-12} | 3.36×10^{-12} | 2.64×10^{-12} |
| 1.25 | 5.15×10^{-12} | 4.08×10^{-12} | 3.26×10^{-12} |
| 1.5 | 5.91×10^{-12} | 4.76×10^{-12} | 3.85×10^{-12} |
| 2 | 7.25×10^{-12} | 5.99×10^{-12} | 4.95×10^{-12} |
| 3 | 9.54×10^{-12} | 8.13×10^{-12} | 6.91×10^{-12} |
| 4 | 1.15×10^{-11} | 1.00×10^{-11} | 8.68×10^{-12} |
| 5 | 1.33×10^{-11} | 1.18×10^{-11} | 1.03×10^{-11} |
| 6 | 1.50×10^{-11} | 1.34×10^{-11} | 1.19×10^{-11} |
| 7 | 1.66×10^{-11} | 1.50×10^{-11} | 1.34×10^{-11} |
| 8 | 1.82×10^{-11} | 1.66×10^{-11} | 1.49×10^{-11} |
| 10 | 2.12×10^{-11} | 1.96×10^{-11} | 1.78×10^{-11} |
| 15 | 2.82×10^{-11} | 2.70×10^{-11} | 2.48×10^{-11} |
| 20 | 3.47×10^{-11} | 3.41×10^{-11} | 3.17×10^{-11} |

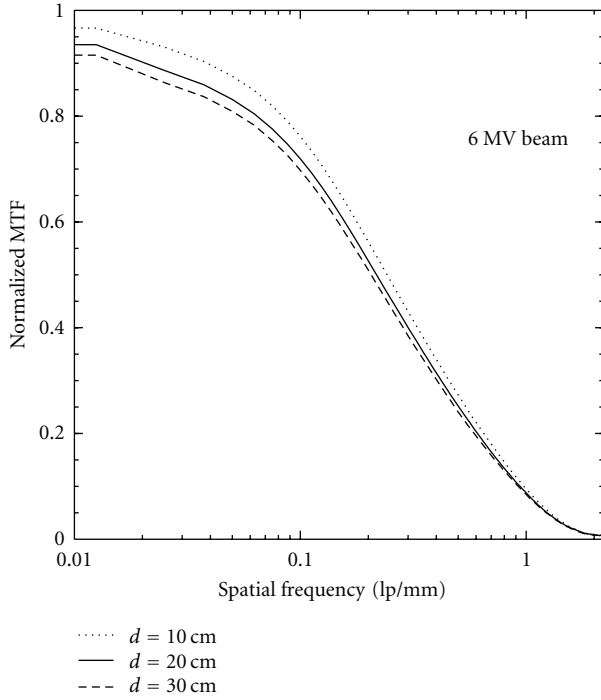
TABLE 2: Detection efficiencies of CPID for three clinical beams. Statistical uncertainty for each value is $\sim 0.8\%$.

| d/cm | 6 MV beam | 10 MV beam | 18 MV beam |
|---------------|-----------|------------|------------|
| 10 | 39.4% | 40.7% | 40.2% |
| 20 | 58.3% | 62.0% | 61.9% |
| 30 | 67.1% | 73.2% | 73.8% |

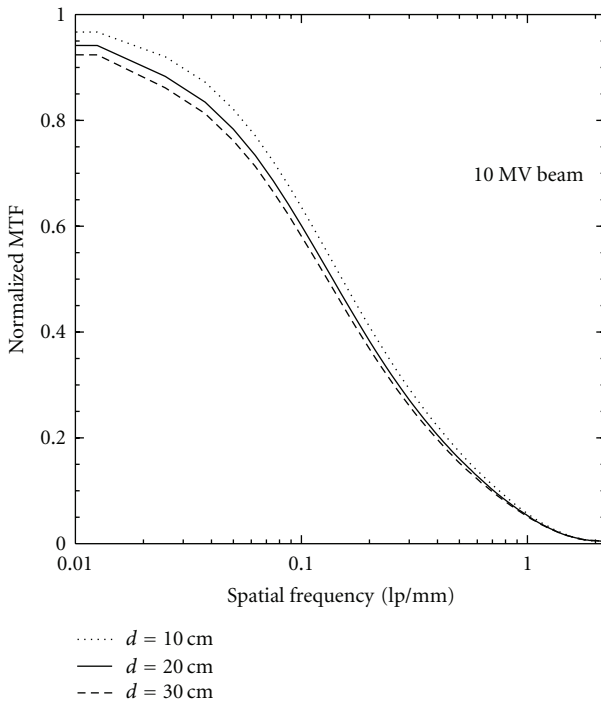
incident X-ray per pixel is shown in Figure 8 as a function of X-ray energy. It can be seen that the number of Cerenkov photons per incident X-ray increases monotonously with X-ray energy for all detector thicknesses.

The total number of the Cerenkov photons per pixel that are generated in the detector and reach the AMFPI per LINAC pulse (~ 0.026 cGy dose to water at the isocentre) [15] is given in Table 3 for various detector thicknesses. These were obtained using a fluence-to-dose conversion factor (8.4×10^{-12} cm²Gy/x-ray) at 6 MV. We note that the total electronic noise per pixel in AMFPIs is typically $\sim 2 \times 10^3$ electrons [17].

3.3. Beam Energy Hardening and Scatter due to the Presence of a Patient. Lower energy photons are attenuated more when passing through a patient, and, as a result the mean energy of the X-ray spectrum exiting the patient increases. This can



(a)



(b)

FIGURE 5: The MTF as a function of spatial frequency for various thicknesses of the proposed CPID. The entrance spectra of X rays from Figure 2 were used in the simulation.

be seen in Figure 2 showing the entrance spectrum and the primary and scatter components of exit beam after traversing a 30 cm thick water phantom. The presence of a patient, in the beam also results in generation of secondary particles

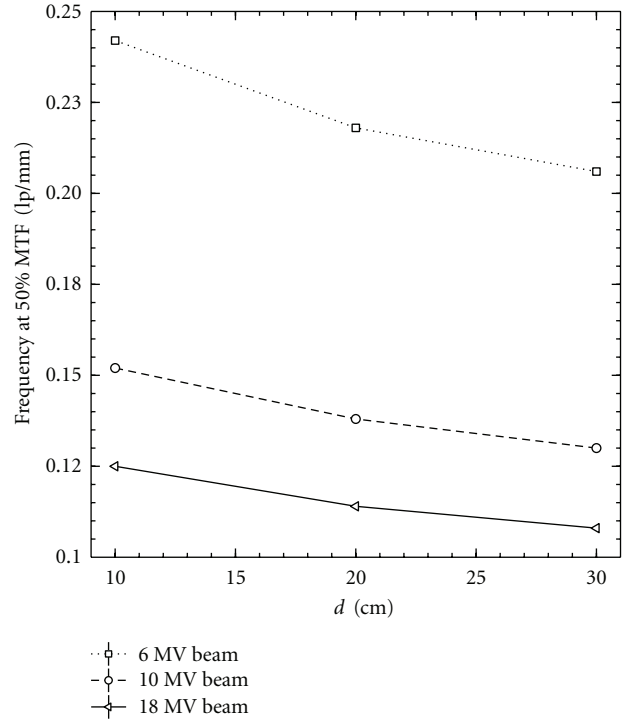


FIGURE 6: The frequency (f_{50}) at 50% of the MTF as a function of detector thickness for different beam energies. The entrance spectra of X rays (see Figure 2) were used in the simulation.

TABLE 3: The total number of Cerenkov photons (that are generated in the detector and reach the AMFPI) per LINAC pulse (~ 0.026 cGy dose-to-water at the isocentre) for a 6 MV beam and various detector thicknesses. Statistical uncertainty for each value is $\sim 0.8\%$.

| Energy (MV) | $d = 10$ cm | $d = 20$ cm | $d = 30$ cm |
|-------------|--------------------|--------------------|--------------------|
| 6 | 1.56×10^5 | 2.41×10^5 | 2.82×10^5 |

TABLE 4: The signal scatter fractions of CPID for three clinical beams. Statistical uncertainty for each value is $\sim 1.8\%$.

| Energy (MV) | $d = 10$ cm | $d = 20$ cm | $d = 30$ cm |
|-------------|-------------|-------------|-------------|
| 6 | 0.19 | 0.17 | 0.17 |
| 10 | 0.18 | 0.16 | 0.15 |
| 18 | 0.17 | 0.15 | 0.14 |

that generally degrade image quality. Figures 9(a) and 9(b) represent the CPID response to the primary and scatter components of the exit beam, respectively, per X-ray incident on water phantom.

Figure 10 gives the signal scatter fraction (SF_{signal} , as defined in (5)) as a function of X ray energy. Except for very low energies ($E_\gamma \leq 0.4$ MeV), where the error is $>100\%$ due to low statistics, the value of SF_{signal} is $\sim 15\text{--}20\%$ and decreases with increase of detector thicknesses.

The signal scatter fractions calculated for three clinical beams (see entrance spectra in Figure 2) incident on a 30 cm thick water phantom are given in Table 4.

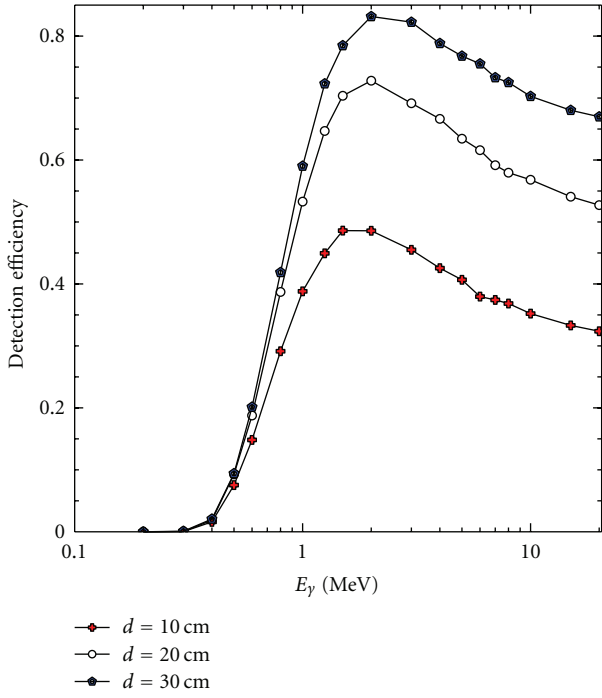


FIGURE 7: The detection efficiency of CPID as a function of incident X-ray energy for various thicknesses.

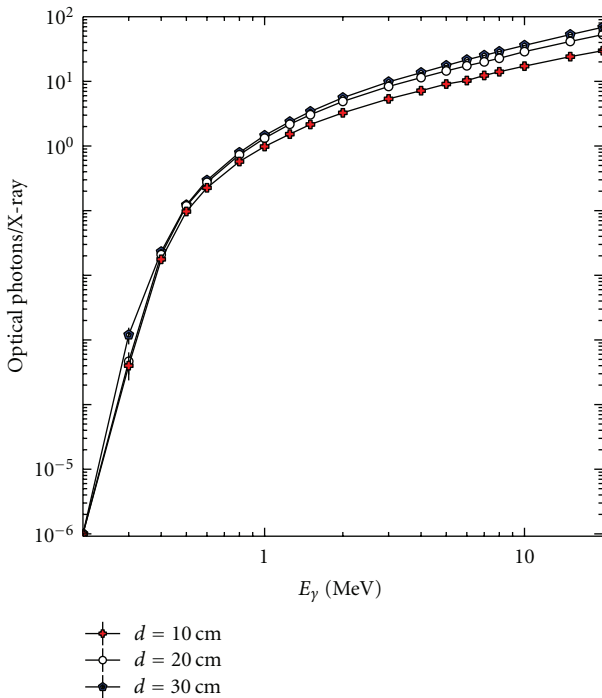
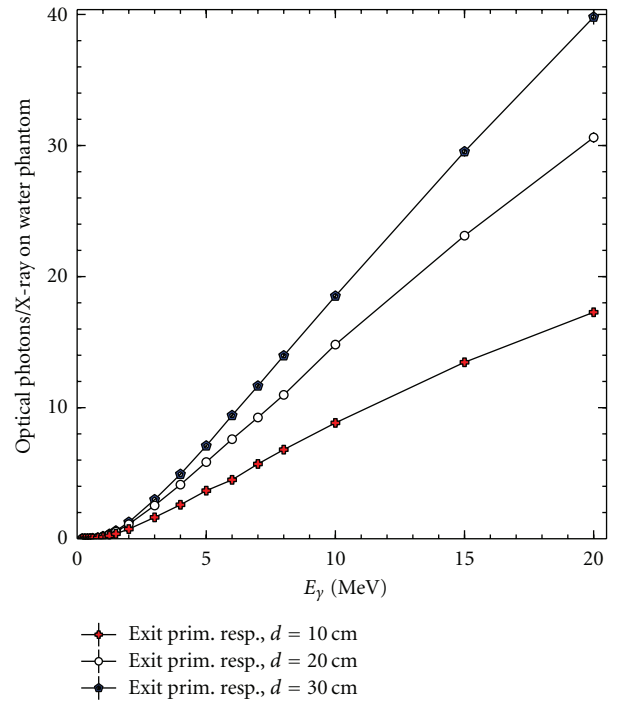
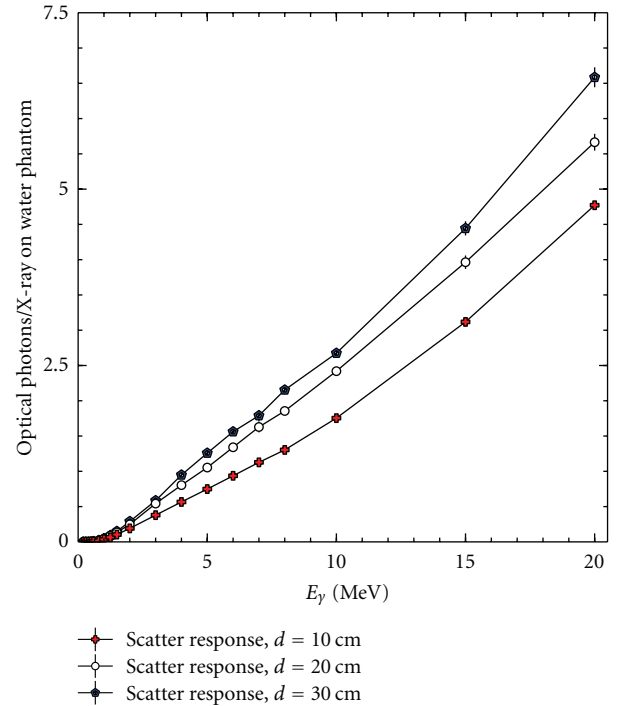


FIGURE 8: The number of Cerenkov photons (that are generated in the detector and reach the AMFPI) per incident X-ray as a function of incident X-ray energy.

Figure 11 shows the normalized spatial (x -direction only) distributions of the detector signal (i.e., distribution of optical photons reaching the AMFPI) for a 30 cm thick CPID



(a)



(b)

FIGURE 9: The number of Cerenkov photons (that are generated in the detector and reach the AMFPI) per X ray incident on the water phantom as a function of X-ray energy.

under irradiation of a 6 MV pencil beam with (open squares) and without (solid circles) the presence of the water slab (see Figure 3). The difference between these two curves is small.

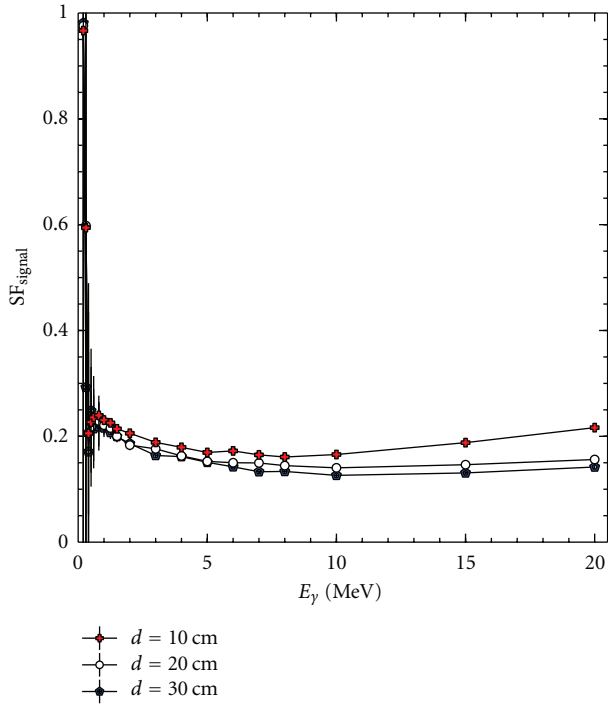


FIGURE 10: The signal scatter fraction for CPID response per pixel as a function of X-ray energy.

TABLE 5: The DQE at zero frequency of CPID for three clinical beams. Statistical uncertainties for each value is $\sim 0.8\%$.

| d/cm | 6 MV beam | 10 MV beam | 18 MV beam |
|---------------|-----------|------------|------------|
| 10 | 20.8% | 22.9% | 23.2% |
| 20 | 31.5% | 36.0% | 37.0% |
| 30 | 37.1% | 43.5% | 45.3% |

3.4. Detective Quantum Efficiency. The zero spatial frequency DQE was calculated from the results of the simulation output using (6) and (7). Figure 12 shows the $\text{DQE}(0)$ as a function of incident beam energy for detector thicknesses of 10, 20, and 30 cm. The $\text{DQE}(0)$ follows the general trend of detection efficiency η (see Figure 7). However, $\text{DQE}(0)$ varies slowly above ~ 2 MeV (compared to detection efficiency). Sufficient number of events has been simulated to provide for a statistical uncertainty at a percent level ($\sim 0.8\%$).

Table 5 lists DQE at the zero spatial frequency simulated for three clinical beams (see entrance spectra in Figure 2). As expected the $\text{DQE}(0)$ of the proposed CPID is more than an order higher than that of current EPIDs [4].

Finally, the spatial frequency dependent detective quantum efficiencies $\text{DQE}(f)$ are shown in Figure 13 for 6 and 10 MV beams at different detector thicknesses.

3.5. Energy Dependence of CPID Dose Response. Figure 14 shows the relative response of the detector per unit dose to water as a function of X-ray energy. It can be seen that the

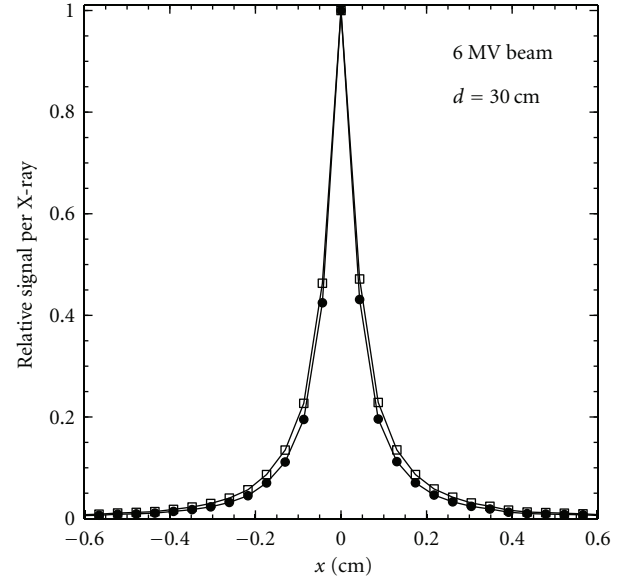


FIGURE 11: Renormalized spatial distributions of the detector signal for a 30 cm thick CPID under irradiation of a 6 MV pencil beam with (open squares) and without (solid circles) the presence of the water slab.

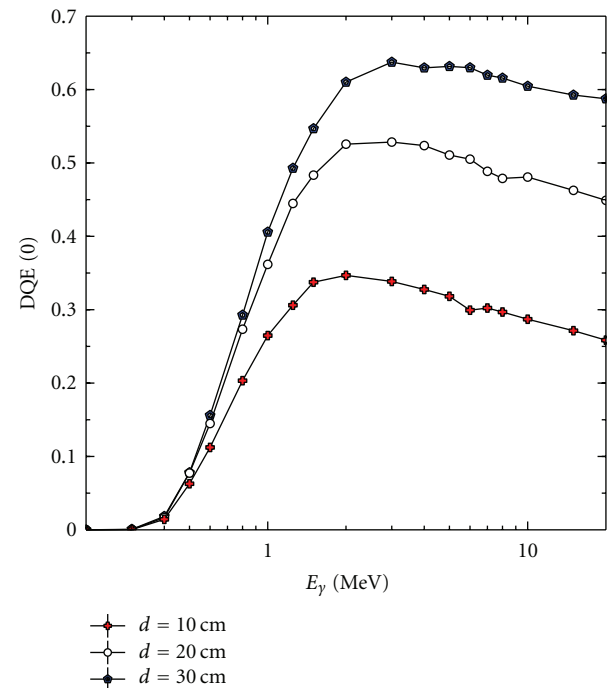


FIGURE 12: The DQE at zero spatial frequency as a function of beam energy for different detector thicknesses.

proposed CPID has lower response to low-energy X rays due to the threshold energy required for generating Cerenkov light. The shape of the energy dependence curve has little dependence on the detector thickness.

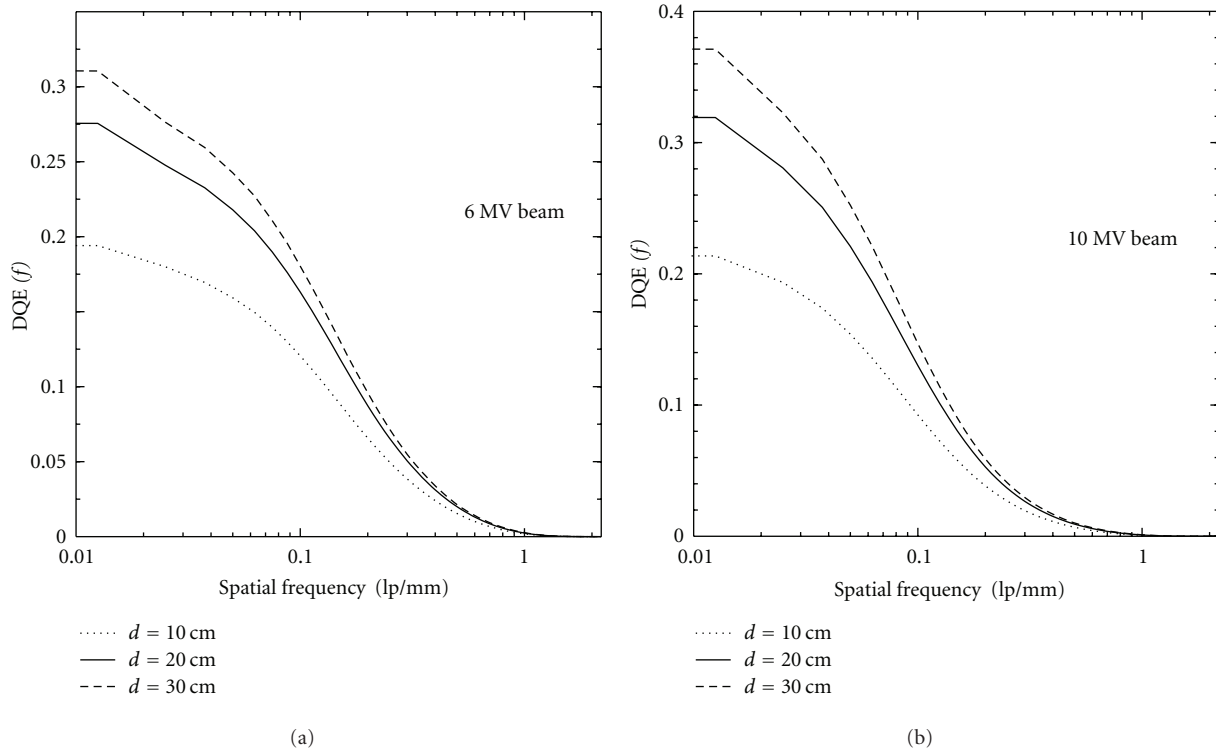


FIGURE 13: The DQE as a function of spatial frequency, obtained from (8), for different detector thicknesses and X-ray spectra.

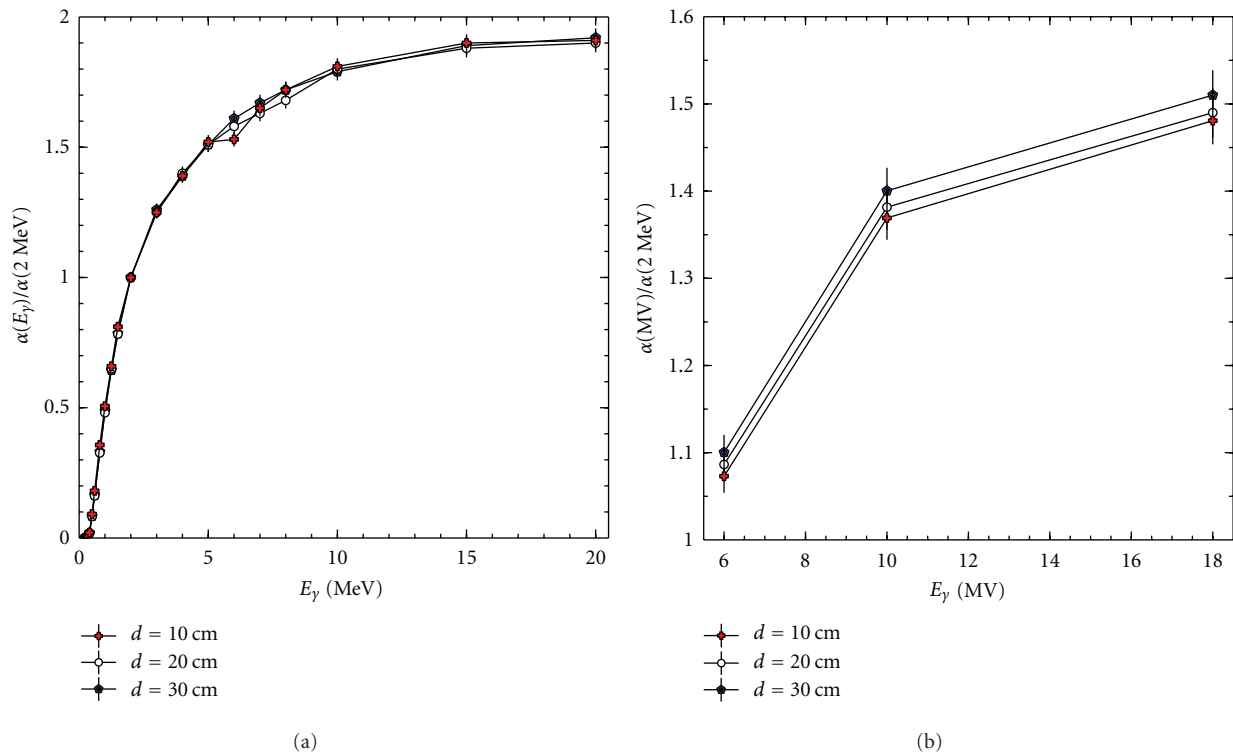


FIGURE 14: Energy dependence curves for the CPID without water phantom. The $\alpha(E_\gamma)/\alpha(2 \text{ MeV})$ curve for monoenergetic beams is shown on the left and $\alpha(\text{MV})/\alpha(2 \text{ MeV})$ curve for polyenergetic beams is shown on the right.

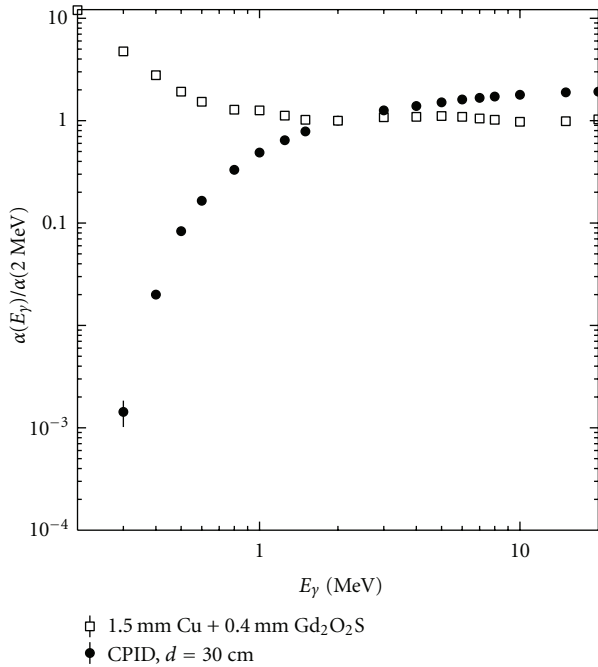


FIGURE 15: Energy dependence of the dose response (for a given dose to water) of a 30 cm thick CPID (solid circles) and that of a conventional Cu plate/phosphor screen system (open squares).

4. Discussion

The main advantage of the proposed CPID is that it can have much higher detection efficiency than current EPIDs. At 6 MV the DQE(0) of CPID can be as high as 37.1%, as compared to $\sim 1\%$ for most current EPIDs. In addition, the energy response of the CPID is also unique. Figure 15 shows the comparison between the CPID (with $d = 30$ cm) and a conventional Cu plate/phosphor screen detector consisting of a $\sim 134 \text{ mg/cm}^2$ $\text{Gd}_2\text{O}_2\text{S}$ phosphor loading (Kodak Lanex fast back) on a 1.5 mm thick copper plate. The energy dependence curve for the Cu plate/phosphor screen was obtained for a given reference dose (to water) from the results of Cremers et al. [22]. In the case of Cu plate/phosphor screen, the reference dose to water is defined as the average dose to a 3 mm thick layer of water at a depth of 3.3 cm in a water phantom with 157 cm SSD [28]. In contrast to the conventional Cu plate/phosphor screen that overresponds to low-energy X rays, the CPID underresponds to X rays below 1 MeV. Since scattered X rays from patients have lower energies than the primary ones and the presence of scattered X rays usually degrade image quality, the underresponse to low energy X rays by the CPID could be advantageous for MV X-ray imaging where no practical antiscatter grid is available. As shown in Table 4, the signal scatter fraction of CPID at 6 MV is 17–19%, which is lower than that ($\sim 35\%$) of a Cu plate/phosphor screen obtained from [24] for the same air gap, X-ray beam energy, and thickness of the scattering material. Thus, the CPID is an antiscatter detector for MV X-ray imaging.

However, there are some disadvantages associated with the proposed detector. The proposed detector could be bulky

and much heavier than current flat-panel-based EPIDs, depending on the thickness chosen. While counterbalancing the large weight of the CPID may require reengineering of the LINAC gantry, the weight issue is common to all high detection efficiency detectors since a large mass of the energy conversion layer is necessary to achieve high detection efficiency. The investigated detector configurations are not expected to be bulkier than a video-based EPID and, thus, would be useable in clinic. In addition, the spatial resolution of the proposed detector would be worse than that of current flat-panel-based EPIDs. This is mainly because (1) more X rays are scattered in our thick detector as compared to that in current flat-panel-based EPIDs [5], and (2) the range of energetic electrons generated by incident X rays in our detector is larger due to the lower density materials used in the CPID. In silica the electron range is approximately 6.8 mm for 6 MV beam and 17 mm for 18 MV beam (based on the value of d_{max} in water [1] scaled by the density of the silica). However, for megavoltage X rays, most energetic electrons generated in the detector are initially moving in the forward direction, that is, in the direction of the incident X rays. In addition, as an energetic electron travels in the detector, it continuously loses its kinetic energy. Once its kinetic energy is below the threshold energy required for Cerenkov radiation, the electron can no longer generate Cerenkov light, and; thus, any further spatial spread of low energy electrons has no effect on the resolution of the CPID. As a result, the resolution of the proposed detector is comparable to that of video-based EPIDs.

5. Conclusions

A Monte Carlo simulation has been conducted to investigate imaging and dosimetric characteristics of a novel design of a megavoltage (MV) X-ray detector for radiotherapy applications. It has been shown that the new design can have a zero-frequency detective quantum efficiency more than an order of magnitude higher than that of current clinical systems and yet a spatial resolution comparable to that of previously developed video-based electronic portal imaging devices. In addition, the proposed detector uses Cerenkov effect to detect MV X rays, and, as a result, it is less sensitive to low-energy X rays (including scattered X rays from patients) than current electronic portal imaging devices.

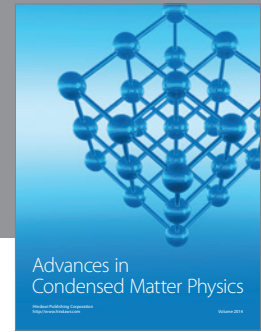
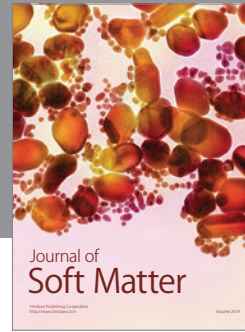
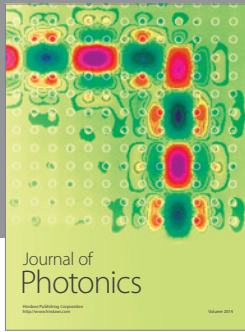
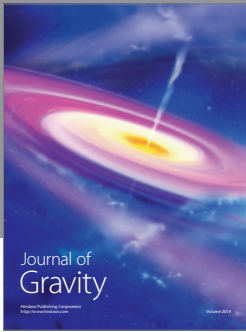
Acknowledgments

This work was supported by the Natural Sciences and Engineering Research Council of Canada (NSERC) and the Canadian Institutes of Health Research (CIHR). The authors also thank Dr. G. Gavalian for providing CPU time on 8 computing cores at Department of Physics, Old Dominion University, VA, USA.

References

- [1] F. M. Khan, *The Physics of Radiation Therapy*, Williams & Wilkins, Baltimore, Md, USA, 2nd edition, 1994.

- [2] E. J. Seppi, P. Munro, S. W. Johnsen et al., "Megavoltage cone-beam computed tomography using a high-efficiency image receptor," *International Journal of Radiation Oncology Biology Physics*, vol. 55, no. 3, pp. 793–803, 2003.
- [3] J. Pouliot, A. Bani-Hashemi, J. Chen et al., "Low-dose megavoltage cone-beam CT for radiation therapy," *International Journal of Radiation Oncology Biology Physics*, vol. 61, no. 2, pp. 552–560, 2005.
- [4] L. E. Antonuk, "Electronic portal imaging devices: a review and historical perspective of contemporary technologies and research," *Physics in Medicine and Biology*, vol. 47, no. 6, pp. R31–R65, 2002.
- [5] G. Pang and J. A. Rowlands, "Development of high quantum efficiency flat panel detectors for portal imaging: Intrinsic spatial resolution," *Medical Physics*, vol. 29, no. 10, pp. 2274–2285, 2002.
- [6] M. A. Mosleh-Shirazi, P. M. Evans, W. Swindell, J. R. N. Symonds-Taylor, S. Webb, and M. Partridge, "Rapid portal imaging with a high-efficiency, large field-of-view detector," *Medical Physics*, vol. 25, no. 12, pp. 2333–2346, 1998.
- [7] J. Ostling, M. Wallmark, A. Brahme et al., "Novel detector for portal imaging in radiation therapy," in *Medical Imaging 2000: Physics of Medical Imaging*, vol. 3977 of *Proceedings of SPIE*, pp. 84–95, February 2000.
- [8] R. Hinderer, J. M. Kapatoes, H. Keller et al., "Development of a new multielement detector system for megavoltage photons," in *Medical Imaging 2002: Physics of Medical Imaging*, vol. 4682 of *Proceedings of SPIE*, pp. 809–818, February 2002.
- [9] A. Sawant, L. E. Antonuk, Y. El-Mohri et al., "Segmented crystalline scintillators: an initial investigation of high quantum efficiency detectors for megavoltage x-ray imaging," *Medical Physics*, vol. 32, no. 10, pp. 3067–3083, 2005.
- [10] T. T. Monajemi, B. G. Fallone, and S. Rathee, "Thick, segmented CdWO₄-photodiode detector for cone beam megavoltage CT: a Monte Carlo study of system design parameters," *Medical Physics*, vol. 33, no. 12, pp. 4567–4577, 2006.
- [11] Y. El-Mohri, L. E. Antonuk, Q. Zhao et al., "Low-dose megavoltage cone-beam CT imaging using thick, segmented scintillators," *Physics in Medicine and Biology*, vol. 56, pp. 1509–1527, 2011.
- [12] G. Pang and J. A. Rowlands, "Development of high quantum efficiency, flat panel, thick detectors for megavoltage x-ray imaging: a novel direct-conversion design and its feasibility," *Medical Physics*, vol. 31, no. 11, pp. 3004–3016, 2004.
- [13] S. Wang, J. K. Gardner, J. J. Gordon et al., "Monte Carlo-based adaptive EPID dose kernel accounting for different field size responses of imagers," *Medical Physics*, vol. 36, no. 8, pp. 3582–3595, 2009.
- [14] D. A. Jaffray, J. J. Battista, A. Fenster, and P. Munro, "Monte Carlo studies of x-ray energy absorption and quantum noise in megavoltage transmission radiography," *Medical Physics*, vol. 22, no. 7, pp. 1077–1088, 1995.
- [15] X. Mei, J. A. Rowlands, and G. Pang, "Electronic portal imaging based on Cerenkov radiation: a new approach and its feasibility," *Medical Physics*, vol. 33, no. 11, pp. 4258–4270, 2006.
- [16] J. V. Jelley, *Cerenkov Radiation and Its Applications*, Pergamon Press, London, UK, 1958.
- [17] J. A. Rowlands and J. Yorkston, "Flat Panel Detectors for Digital Radiography," in *Handbook of Medical Imaging*, L. V. M. Richard, B. Jacob, and L. K. Harold, Eds., pp. 223–328, SPIE Press, 2000.
- [18] J. M. Boudry and L. E. Antonuk, "Radiation damage of amorphous silicon, thin-film, field-effect transistors," *Medical Physics*, vol. 23, no. 5, pp. 743–754, 1996.
- [19] K. Tanioka, J. Yamazaki, K. Shidara et al., "Avalanche-mode amorphous selenium photoconductive target for camera tube," in *Advances in Electronics and Electron Physics*, B. L. Morgan, Ed., vol. 74, pp. 379–387, Academic Press, 1988.
- [20] S. Agostinelli, J. Allison, K. Amako et al., "GEANT4—a simulation toolkit," *Nuclear Instruments and Methods in Physics Research A*, vol. 506, no. 3, pp. 250–303, 2003.
- [21] J. T. Dobbins, "Effects of undersampling on the proper interpretation of modulation transfer function, noise power spectra, and noise equivalent quanta of digital imaging systems," *Medical Physics*, vol. 22, no. 2, pp. 171–182, 1995.
- [22] F. Cremers, T. Frenzel, C. Kausch, D. Albers, T. Schönborn, and R. Schmidt, "Performance of electronic portal imaging devices (EPIDs) used in radiotherapy: image quality and dose measurements," *Medical Physics*, vol. 31, no. 5, pp. 985–996, 2004.
- [23] H. Fujita, D. Y. Tsai, T. Itoh et al., "A simple method for determining the modulation transfer function in digital radiography," *IEEE Transactions on Medical Imaging*, vol. 11, no. 1, pp. 34–39, 1992.
- [24] D. A. Jaffray, J. J. Battista, A. Fenster, and P. Munro, "X-ray scatter in megavoltage transmission radiography: Physical characteristics and influence on image quality," *Medical Physics*, vol. 21, no. 1, pp. 45–60, 1994.
- [25] R. K. Swank, "Absorption and noise in x-ray phosphors," *Journal of Applied Physics*, vol. 44, no. 9, pp. 4199–4203, 1973.
- [26] C. E. Dick and J. W. Motz, "Image information transfer properties of x-ray fluorescent screens," *Medical Physics*, vol. 8, no. 3, pp. 337–346, 1981.
- [27] M. Lachaine and B. G. Fallone, "Monte Carlo detective quantum efficiency and scatter studies of a metal/a-Se portal detector," *Medical Physics*, vol. 25, no. 7, pp. 1186–1194, 1998.
- [28] B. M. C. McCurdy, K. Luchka, and S. Pistorius, "Dosimetric investigation and portal dose image prediction using an amorphous silicon electronic portal imaging device," *Medical Physics*, vol. 28, no. 6, pp. 911–924, 2001.



Hindawi

Submit your manuscripts at
<http://www.hindawi.com>

